

A Physical Approach for the Observation of Oil Spills in SAR Images

Maurizio Migliaccio, *Senior Member, IEEE*, Massimo Tranfaglia, *Student Member, IEEE*, and Stanislav A. Ermakov

Abstract—In this paper, a physical approach to support oil spills observation over synthetic aperture radar (SAR) images is presented. Electromagnetic model is based on an enhanced damping model that takes into account oil viscoelastic properties and wind speed. As a matter of fact, a multisensor approach is considered and a constant false alarm rate (CFAR) filter is used to minimize speckle effect. A set of experiments is presented and discussed. They show that oil spill processing is effective over single-look SAR images using mean input data.

Index Terms—Backscattering model, edge detector, oil spills, SAR, scatterometer.

I. INTRODUCTION

OIL sea pollution is matter of great concern. In fact, about 90% of crude oil and oil products are transported across the globe by oil tankers. Further, part of it is extracted by offshore platforms and most of the refineries are along coasts. All this unavoidably generates sea pollution.

Such pollution can be due to major disasters, such as oil tankers sinking, but even to chronic events such as illegal tank cleaning or bilge pumping. In any case, it is impressive to note that the amount of oil spilled annually worldwide has been estimated at a level greater than 4.5 million tons, equivalent to one full-tanker disaster every week [1]–[4].

Oil pollution causes marine ecological disasters that result in great damages of the quality and productivity of marine environment and involve great expenses in clear-up operations [1]. The impact of oil depends also on the viscosity, toxicity, and the amount of oil, as well as on the sensitivity of the living organisms and the duration of exposure to the oil [2]. The animals and plants most at risk are those that come into contact with the contaminated sea surface: marine mammals; reptiles and some species of birds; marine life on shorelines; and animals and plants in mariculture facilities. Impact of oil pollution

Manuscript received June 30, 2004; revised March 25, 2005; accepted May 1, 2005. This work was supported in part by the ASI R/I/200/02 contract, fondi locali di ricerca (ex 60%, year 2003, cap. 12026505), RFBR funds (Project 02-05-62102), and INTAS funds (Project 03-51-4987). Research work was developed at the Laboratorio di Telerilevamento Ambientale, Università degli Studi di Napoli “Parthenope.” Associate Editor: R. Garello.

M. Migliaccio is with the Dipartimento per le Tecnologie, Università degli Studi di Napoli “Parthenope,” Napoli 80133, Italy (e-mail: maurizio.migliaccio@uniparthenope.it).

M. Tranfaglia was with the Università degli Studi di Napoli “Parthenope,” Napoli 80133, Italy. He is now with the Dipartimento di Ingegneria, Università degli Studi del Sannio, Benevento 82100, Italy (e-mail: massimo.tranfaglia@unisannio.it).

S. A. Ermakov is with the Institute of Applied Physics, Russian Academy of Sciences, Nizhny Novgorod 603600, Russia (e-mail: stas@hydro.appl.sci-nnov.ru).

Digital Object Identifier 10.1109/JOE.2005.857518

is not only related to the quantity but also on location, season, ocean depth, meteorological, and oceanic conditions. Potential damages and the difficulty to restore these habitats and biological natural resources stimulated a public awareness in order to protect sea trustee [2]. Therefore, stricter national and international laws have been established.

The capability to detect an oil spill is fundamental to effectively plan countermeasures and minimize the effect of pollution. A successful operational system depends on a rapid and reliable warning capability.

Classical visual monitoring systems operated by coast guard personnel are limited in space and time. Therefore, classical systems do not match the requirements mentioned above.

In order to enhance oil spill observation, remote sensing measurements can be exploited. In particular, use of satellite remote sensing measurements is recognized nowadays as an efficient tool, in conjunction with standard observation techniques, to ensure synoptic oil spill monitoring. In fact, satellite remote sensing measurements are available at moderate cost with respect to *in situ* classical observation. However, it has to be noted that physical expertise must be used to interpret remote sensing data, and this affects the actual overall cost.

Within such a framework, the most suitable sensor is the synthetic aperture radar (SAR). It is an active coherent band-limited microwave high-resolution remote sensing sensor capable to provide wide-area surveillance and day and night measurements, (almost) independently from atmospheric conditions, which is very advisable for the application in question. Physically, the sea scattering mechanism, which governs the electromagnetic wave–ocean surface interaction, is the Bragg scattering mechanism. In other words, the small perturbation model (SPM) applies. Since oil spills cause a dampening of surface short waves, which are at the basis of the Bragg scattering mechanism, oil spills appear as dark patches in SAR images.

Actually, oil spills detection over SAR images is not at all an easy task. In fact, other physical phenomena can also generate dark patches [5], [6] and SAR images are affected by multiplicative noise known as speckle [7].

Dark patches not related to oil spill are known as look-alikes. They can be due to low wind speed areas, internal waves, biogenic films, grease ice, wind front areas, areas sheltered by land, rain cells, current shear zones, and up-welling zones.

Since the most remarkable ones are low wind speed areas, the knowledge of wind speed has a great relevance in oil spills detection. As a matter of fact, the reduction of the sea surface roughness and, consequently, of the friction velocity, due to the presence of a surfactant on sea surface, influences the transfer of energy and momentum from wind to the waves. Consequently,

the action balance equation is modified, involving also a change of the wind wave growth. Although the processes responsible for the transfer of energy and momentum from the wind to the waves have not been fully understood, especially in the environmental conditions present at the sea, the knowledge of the physics at the basis of damping mechanism for proper oil spills detection is very important to reduce the number of false alarms. However, it has to be noted that with high wind speed, few oil spills are detected over SAR images [5].

Moreover, SAR images are affected by speckle noise, which is due to the coherent and narrow-band nature of the SAR system and makes very difficult oil spill detection. Speckle can be reduced by a processing technique known as multilook [7]. On one side, multilook enhances interpretability, and this is fundamental for automatic or semiautomatic oil spill processing. On the other side, multilook generates SAR images at coarser spatial resolution, and this hampers small-size oil spill detection. On the operative perspective, multilook data storage as well as processing is less demanding because of data reduction. Further, simple filters based on the gradient operator can be applied.

A detailed state-of-art of oil spill observation over SAR images is well reported in [5] and [6].

Several semiautomatic oil spills detection procedures based on SAR images have been presented in literature [9]–[21]. These oil spill processing techniques are semiautomatic since a key role is played by a human expert who selects the SAR image area to be processed and assists interpretation. The automatic processing is based on gradient-like filters to detect oil spills over multilook SAR images. Multilook SAR images with spatial resolution of about $100 \text{ m} \times 100 \text{ m}$ are generally used, e.g., [15]. After a candidate oil spill has been detected, some key features are evaluated to perform classification [5], [6]. The most popular features are morphological, namely the perimeter and the area and/or their function [5], [6]. In order, to enhance the capability of these techniques to distinguish an oil spill from a look-alike and to reduce the number of false alarms, the need to take into account the local wind field is recognized nowadays [5], [6], [21]–[24].

First attempts to exploit the wind speed are reported in [14] and [24]. In [14], an empirical but effective approach is proposed, while in [24], the wind speed is obtained by an external source and incorporated into the model.

In this paper, a new oil spill processing over SAR images based on physical modeling is presented. The observable damping over SAR image is modeled by means of SPM, which incorporates the oil spill damping model and the Ermakov *et al.* studies [24]–[26]. Consequently, a physical threshold value is estimated by means of the physical oil spill parameters and the wind speed. To make the processing feasible to operational use, mean input data are used. In particular, scatterometer wind fields are taken into account. Wind fields have been acquired by National Aeronautics and Space Administration (NASA) SeaWinds scatterometer. They are provided on an approximately $0.25^\circ \times 0.25^\circ$ global grid. Separate maps are provided both for ascending and descending pass and rain probability is also included as an indicator of wind field reconstruction accuracy [27].

In order to process single-look SAR images, i.e., at full resolution, a filter appropriately tailored to deal with speckle is con-

sidered. It is the ratio of average (ROA) filter belonging to the class of constant false alarm rate (CFAR) filters [28], [29].

The ROA filter is a simple filter and is, therefore, very attractive for operational use.

In summary, the new oil spill processing over full-resolution SAR images is physically based, needs mean input data, and is a simple filter to be run. Experimental results are based on $0.2 \text{ m} \times 0.5 \text{ m}$ airborne *X*-band SAR images provided by the Telaar consortium. SAR images are relevant to the Galicia mission.

Results show the effectiveness of the processing in discriminating between oil spills and look-alikes and the capability to detect small-size oil spills.

The remainder of the paper is organized as follows. In Section II, the physical damping background is provided. In Section III, the observable damping is presented. It is based on the SPM scattering model and on the oil damping theory of Section II. In Section IV, the physically based oil spill processing over single-look SAR images is described. In Section V, the experimental results are presented and discussed. In Section VI, the paper results are summarized and conclusions are drawn.

II. PHYSICAL BACKGROUND

In this section, we present the physical background that is at the basis of our study. Let us consider the fundamental action balance equation [30]

$$\frac{dN(\mathbf{K})}{dt} = \frac{\partial N(\mathbf{K})}{\partial t} + \mathbf{c}_g \cdot \nabla N(\mathbf{K}) = Q(\mathbf{K}) = Q_w + Q_{nl} - Q_d \quad (1)$$

where \mathbf{K} is the wavenumber vector and $N(\cdot)$ is the action spectral density defined as

$$N(\mathbf{K}) = \frac{\Omega}{K} W(\mathbf{K}) = c_p W(\mathbf{K}). \quad (2)$$

$W(\mathbf{K})$ is the directional spectrum and Ω is the angular frequency of the wave defined by the dispersion relationship

$$\Omega^2 = gK \left(1 + \frac{K^2}{K_m^2} \right) \quad (3)$$

where g is the acceleration of gravity, $K_m = (\rho g / \tau)^{1/2}$, ρ is the sea water density, and τ is the surface tension.

Equation (1) states that the energy content of wave propagating at the group velocity \mathbf{c}_g is modified by source terms Q_w , Q_{nl} , and Q_d , which represent the spectral distribution of the energy input furnished by the wind, by the nonlinear wave–wave interaction, and subtracted by dissipation, respectively. This latter term is constituted by the terms Q_v and Q_{br} that represent the energy losses due to viscous dissipation and wave breaking, respectively.

Equation (1), for the case in question, is generally simplified as [23]

$$Q(\mathbf{K}) = Q_w + Q_{nl} - Q_d = 0. \quad (4)$$

Actually, the solution of (4) is not at all straightforward since the exact analytical expression of $Q(\cdot)$ is unknown. Hence, some physical assumptions are made to get the expression of $Q(\cdot)$. Let us now describe the various source terms.

The wind source term Q_w is here considered as [22]

$$Q_w = \beta \cdot N(\mathbf{K}). \quad (5)$$

The wind wave growth rate β for moderate wind regimes is described by a simple empirical expression [31]

$$\beta = B(\cos \varphi)^{2d} \left(\frac{u_*}{c_p} \right)^2 \Omega \quad (6)$$

where $B = 0.04$, $d = 0.5$, φ is the sea wave azimuth angle, i.e., the angle between wind and wave propagation direction, c_p is the phase speed, and u_* is the friction velocity.

The rate of energy transfer to waves is dependent on the profile of mean flow very close to the interface. If a neutral atmosphere is considered, i.e., such that there is no thermal exchange between air and water, the wind speed U at a given height z above the surface is related to the wind friction velocity u_* by [32]

$$U(z) = \frac{u_*}{0.4} \ln \left(\frac{z}{z_0} \right). \quad (7)$$

In general, the roughness length z_0 depends on the sea state and, thus, on the wind velocity. Some relationships have been investigated to relate z_0 to u_* . In this study, we consider the new result obtained by Donelan [33], thus

$$z_0 = 0.000037 \frac{U_{10}^2}{g} \left(\frac{c_p}{U_{10}} \right)^{-0.9} \quad (8)$$

where U_{10} is the wind speed at 10 m of height.

If gentle wind regimes are in question, the expression for the wind wave growth coefficient becomes [25]

$$\hat{\beta} = 10^{-2} \cdot K u_* \cos \varphi \cdot \left[1 + 1.6 \frac{K u_*}{\Omega} \cos \varphi \right] \times \left\{ 1 - \exp \left[8.9 \left(\frac{K u_*}{\Omega} - 0.03 \right)^{\frac{1}{2}} \right] \right\}. \quad (9)$$

Let us now consider the dissipation terms.

Linear viscous dissipation in (1) can be described as [22]

$$Q_v = \gamma N(\mathbf{K}) \quad (10)$$

where the damping coefficient γ for the gravity–capillary waves in the presence of an elastic surface film can be written as [26]

$$\gamma = 2\nu K^2 + \frac{\gamma_m}{2} \left| \frac{U_r}{U_p} \right|^2. \quad (11)$$

The first term on the right-hand side of (11) is the well-known expression for the gravity–capillary waves damping in a fluid with a clean surface where ν is the kinematic viscosity of the sea water. The other term describes an additional damping due to the oil film in which γ_m is given by [26]

$$\gamma_m = \left(\frac{\nu \Omega K^2}{2} \right)^{\frac{1}{2}}. \quad (12)$$

The ratio of the amplitudes of the vortex and potential components of gravity–capillary waves is defined by [26]

$$\left| \frac{U_r}{U_p} \right|^2 = 2 \frac{e^2}{1 - 2e + 2e^2} \quad (13)$$

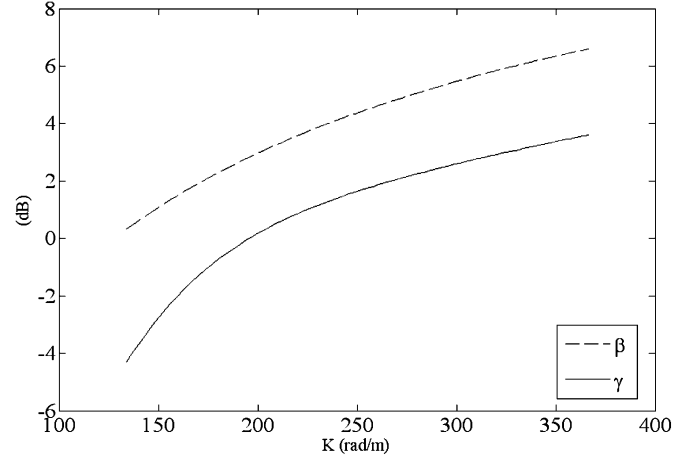


Fig. 1. Plots of the wind wave growth coefficient β and viscous dissipation coefficient γ as a function of K for fuel oil no. 6 and at wind speed of 7 m/s. The curves are obtained using (6) and (11) in which the film elasticity is set to 0.01 N/m.

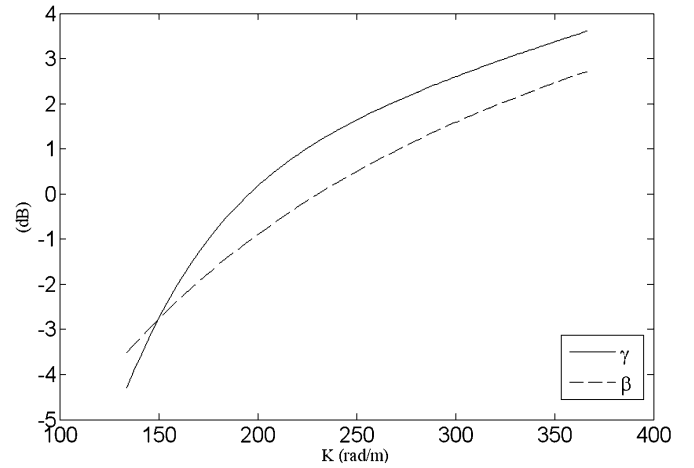


Fig. 2. Plots of the wind wave growth coefficient β and viscous dissipation coefficient γ as a function of K for fuel oil no. 6 and at wind speed of 4 m/s. The curves are obtained using (6) and (11) in which the film elasticity is set to 0.01 N/m.

where $e = E/E_0$ is the dimensionless elasticity and

$$E_0 = \frac{\sqrt{2\eta\rho\Omega^3}}{K^2} \quad (14)$$

where η is the dynamic viscosity of the sea water.

We note that although (11) is valid for purely elastic films, it is often applicable to thin (monomolecular) films, since surface film viscosity is usually small. When damping of thick crude oil film is in question, one may think to consider appropriately tailored damping coefficient modeling. Unfortunately, the present state of the art does not provide detailed characterization of such oil films. Undergoing research activity is currently developed at Institute of Applied Physics (IAP), Russian Academy of Sciences, Nizhny Novgorod, Russia.

In Fig. 1, the plots of β and γ for an oil film characterized by $E = 0.01$ N/m and a wind speed $U = 7$ m/s are shown. In Fig. 2, the case relevant to $U = 4$ m/s is shown. In the latter case, the viscous damping coefficient is greater than the wind wave growth coefficient. This is typical of gentle wind regimes and the model must be adjusted accordingly [25].

If gentle wind regimes are in question, the following expression for the viscous damping coefficient is used [25]

$$\hat{\gamma} = 2\nu K^2 \cdot \frac{\frac{2\nu K^2}{\Omega} - \sqrt{\frac{2\nu K^2}{\Omega} \cdot \frac{EK^3}{\rho\Omega^2}} - \left(\frac{EK^3}{\rho\Omega^2}\right)^2}{2\sqrt{\frac{2\nu K^2}{\Omega}} \cdot \frac{EK^3}{\rho\Omega^2} + 2\left(\frac{EK^3}{\rho\Omega^2}\right)^2}. \quad (15)$$

Let us now move to consider the nonlinear term in (1). Its power-law approximation is [22]

$$Q_{\text{br}} = a [K^4 W(\mathbf{K})]^n \Omega N(\mathbf{K}) \quad (16)$$

where a is an empirical coefficient. Donelan and Pierson suggested to use (16) to phenomenologically describe the surface wave breaking processes [22], [33].

Considering the spectrum of the wind waves under equilibrium state ($dN/dt = 0$) from (1), we have [22]

$$W(\mathbf{K}) \propto \sqrt{\frac{|\cos \varphi| u_*^2}{gK^7}}. \quad (17)$$

In [22] and [33], a is set to 2^n where n is given by

$$n = (n_1 - n_2) \left| 2 - \frac{g + 3TK^2}{g + TK^2} \right|^d + n_2, \quad (18)$$

where T is the ratio between the surface tension τ and the density ρ ; n_1 , n_2 , and d are dimensionless parameters determined from gravity wave observations and from radar backscatter measurements of gravity–capillary waves [31].

III. SCATTERING BACKGROUND

In this section, the observable damping model, i.e., the ratio of the normalized radar cross sections (NRCS) σ^o in the slick-free and the slick-covered cases, is presented. On this purpose, the suitable and popular approximation of the Huygens–Fresnel scattering integral is provided by the SPM [34], [35].

For slick-free water surface, σ^o is given by [35]

$$\sigma_{\text{tr}}^o = \frac{4}{\pi} k^4 \cos^4 \theta |\alpha_{\text{tr}}|^2 W(\mathbf{K}) \quad (19)$$

where the subscripts $t(r)$ stands for transmitted (received) electromagnetic polarization, k is the electromagnetic wavenumber, θ is the local incidence angle evaluated according to [36], and α_{tr} are the modified Fresnel coefficients [34], [35]. A proper description of α_{tr} can be found in [34] and [35].

Since the thickness of the oil spill is very small compared to the microwave penetration depth at the sea, it is appropriate to consider the term α_{tr} unaffected by the presence of oil spill [34], [35], [37]. Accordingly, the observable damping is given by

$$\frac{\sigma_f^o}{\sigma_c^o} = \frac{N_f(\mathbf{K})}{N_c(\mathbf{K})} = \frac{\beta_c - \gamma_c}{\beta_f - \gamma_f} \cdot \frac{Q_{\text{br}}^f - Q_{\text{nl}}^f}{Q_{\text{br}}^c - Q_{\text{nl}}^c} \quad (20)$$

in which the symbols f and c are for slick-free and slick-covered sea surface, respectively, and (4), (5), (10), and (19) have been used.

In order to fully describe the observable damping, we need to model the second factor appearing at the right-hand side of (20). Its analytical expression is unavailable, and some approximations have been suggested in literature [22]–[24]. In [22], an

expression has been obtained by adjusting the model to measurements; in [24], some physical arguments have been given in support of the proposed expressions. According to [22], we have

$$\frac{Q_{\text{br}}^f - Q_{\text{nl}}^f}{Q_{\text{br}}^c - Q_{\text{nl}}^c} = A(\varphi, n_f, n_c) \cdot K^{\frac{(n_f - n_c)}{2}} \quad (21)$$

where

$$A(\varphi, n_f, n_c) = \frac{a_f}{a_c} \cdot r^{-n_c - 1} \cdot u_*^{n_f - n_c} \left(\sqrt{\frac{|\cos \varphi|}{g}} \right)^{n_f - n_c}. \quad (22)$$

The parameter r is the ratio of the friction velocities for slick-covered and slick-free surfaces and measures the reduction of friction velocity due to the oil spill.

Combining (18) and (21), a proper description of the nonlinear and wave breaking terms is obtained [22]

$$\frac{Q_{\text{nl}}^f - Q_{\text{br}}^f}{Q_{\text{nl}}^c - Q_{\text{br}}^c} = r^{\Delta n - 4} \left(2u_* \sqrt{\frac{|\cos \varphi| K}{g}} \right)^{\Delta n} \quad (23)$$

where $\Delta n = n_f - n_c$.

Finally, the observable damping at moderate wind regimes is obtained

$$\frac{\sigma_f^o}{\sigma_c^o} = \frac{N_f(\mathbf{K})}{N_c(\mathbf{K})} = \frac{\beta_c - \gamma_c}{\beta_f - \gamma_f} \cdot r^{\Delta n - 4} \left(2u_* \cdot \sqrt{\frac{|\cos \varphi| K}{g}} \right)^{\Delta n}. \quad (24)$$

At a gentle breeze, the viscous dissipation can be greater than the wind input. Equation (24) becomes zero when β_c and γ_c are equal (see Fig. 2). Therefore, the evaluation of the theoretical damping ratio is possible only for the case in which the wind input is greater than the viscous dissipation. At gentle wind regimes, the breaking wave term and the nonlinear term in (4) can be neglected [25].

Using (4), (9), and (15), the observable damping at gentle wind regimes is obtained [25]

$$\frac{\sigma_f^o}{\sigma_c^o} = \frac{N_f(\mathbf{K})}{N_c(\mathbf{K})} = \frac{\hat{\gamma}_c - \hat{\beta}_c}{\hat{\gamma}_f - \hat{\beta}_f}. \quad (25)$$

Equation (25) can be further simplified at very low wind regimes in which $\hat{\beta}$ can be neglected [25].

IV. SAR IMAGE PROCESSING

In this section, we present the SAR image processing that is used to detect oil spills. Two key issues need to be properly considered: 1) speckle; and 2) edge filtering.

Speckle arises from the coherent and narrow-band nature of sensor. It causes random constructive and destructive interference and, hence, random bright and dark interpixel variation over macroscopically homogeneous areas. Speckle can be reduced at the expenses of spatial resolution by a processing known as multilook. Multilook processing can be implemented in accordance to two general techniques.

The first technique divides the available bandwidth of the SAR system into subbands. Each subband is used to generate a lower resolution SAR image. Then the independently generated images are averaged. The effectiveness of the multilook processing is measured by the equivalent number of looks (ENL),

which, in this case, is directly related to the number of independent SAR images considered.

In the second technique, the process starts from the full-resolution, i.e., single-look, SAR image. Then, over the SAR image, a weighting filtering is applied to smooth out the speckle. Again, the ENL is used to measure the effectiveness of the multilook processing.

In practice, the first technique can be applied if SAR raw signal data are available, while the second one can be applied even having at disposal only single-look SAR images [7], [34].

With respect to oil spill detection over SAR images, it is common practice to use multilook images. In fact, multilook processing reduces speckle noise and increase interpretability [34]. In practice, SAR multilook images of about $100 \text{ m} \times 100 \text{ m}$ are used, e.g., [15]. Additionally, use of multilook SAR image facilitates gradient-like analysis and alleviates time requirements since it reduces the amount of data to be processed. Obviously, the loss of spatial resolution may hamper the detection of small oil spills.

Edge detection, is an essential tool to identify and classify an oil spill in SAR images.

Edge detection is the process to locate the edge pixels, while edge enhancement is the process that increases the contrast between the edges and the background so that the edges are more visible [38]. In general, the efficiency of edge detection, noise sensitivity, and computational efficiency are competing needs that must be properly considered to select the most suitable edge operator given the geophysical application.

Different edge detectors, sensitive to the grey tone variation, are used for oil spills detection. In particular, gradient or gradient-like edge filters are usually used [5]–[21].

These filters are simple: At a given point, they evaluate a function of the difference between the two pixels contiguous at the point. An extension of this operator, less sensitive to the noise, is defined by the difference of the average pixel values of two nonoverlapping neighborhoods on opposite sides of the point. The value of the difference is assigned to the point and the image gradient is computed [38]. Unfortunately, the presence of speckle makes this analysis ineffective [28], [29]. In order to overcome such an intrinsic limitation, it is common practice, in semiautomatic SAR image analysis procedures for oil spills detection, to consider multilook SAR images [5]–[21].

An alternative approach is possible, and it is pursued in this paper. In order to mitigate speckle noise, without hampering the SAR spatial resolution, a filter adapted to the nature of the speckle noise is considered. A simple filter belonging to the class of CFAR edge detectors developed specifically for SAR images is used [28], [29]. The ROA is implemented to detect oil spills over SAR images.

The ROA filter is also attractive in terms of computation time and, therefore, has been selected for this real-time oriented procedure. The ROA filter is defined as the ratio of the average (arithmetic average for a power image, quadratic for an amplitude one) of pixel values of two nonoverlapping neighborhoods on opposite sides of the point [28], [29]. If the ratio operator

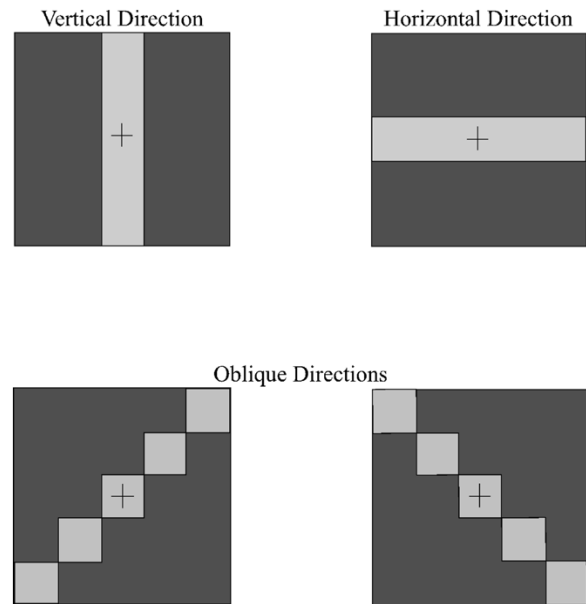


Fig. 3. Relevant to the ROA filter. + indicates the application point; the two dark zones are the nonoverlapping regions.



Fig. 4. Learjet 35A used for X-band SAR observations.

TABLE I
SAR SYSTEM PARAMETERS

Frequency	9.35 GHz
Polarization	HH
Mean incidence angle at near range	20°
Mean incidence angle at far range	70°
Platform altitude range	6000-8000 m
Slant range resolution	0.2 m
Azimuth resolution	0.5 m

TABLE II
FUEL OIL NO. 6 MEAN PARAMETERS

Density ρ	984 Kg/m ³
Surface tension τ	0.0307 N/m
Elasticity E	0.01 N/m

is computed over two homogeneous neighborhoods of M independent pixels, its conditional probability density function (pdf) is given by [28]

$$p\left(\frac{R}{P_1}, P_2\right) = \frac{m\Gamma(2ML)}{\Gamma(ML)^2} \left[\frac{\left(\frac{P_1}{P_2}\right)^{ML}}{\left(R^m + \frac{P_1}{P_2}\right)^{2ML}} \right] R^{mML-1} \quad (26)$$

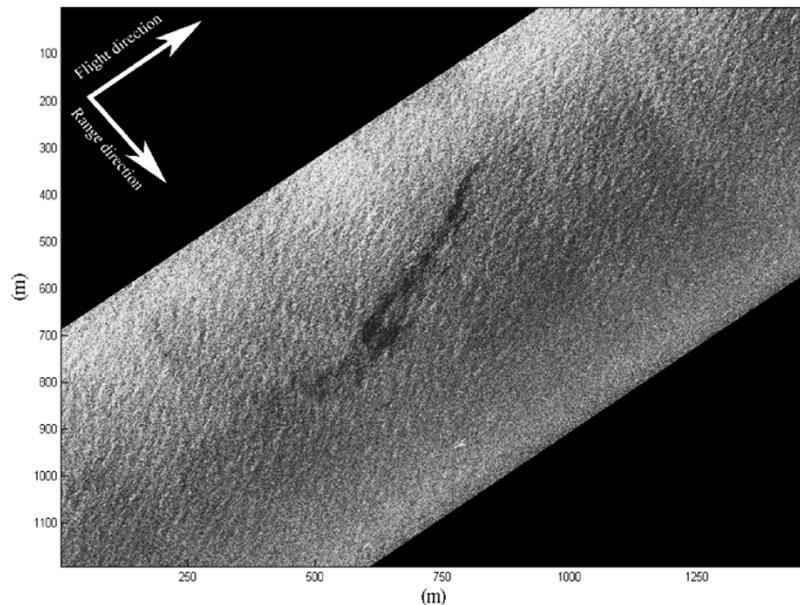


Fig. 5. SAR image acquired at X -band on 25 January 2003 at 1255 UTC, flight altitude 28 000 ft, and ground speed 150 m/s (courtesy of Telaer consortium).

where the ratio random variable $R \in [0, +\infty]$ is defined as $R = P_1/P_2$, in which P_1 and P_2 are the mean power of two neighborhoods assumed to be homogeneous, m is equal to 1 for a power image and 2 for an amplitude image, $M = m(m - 1)/2$, L is the number of looks, and $\Gamma(\cdot)$ is the Eulerian gamma function [39].

Equation (26) shows that $p(R)$ depends on the mean power ratio and not on the two power levels as in the gradient case [28], [29]. Two decision thresholds T_1 and T_2 must be fixed for a given false alarm probability P_{fa} . The considered point is assigned to the edge class if $R < T_1$ or $R > T_2$, and to the homogeneous class in the other cases. Hence, the use of the ROA edge detector depends on the choice of T_1 and T_2 ($T_1 \leq 1$ and $T_2 \geq 1$). In order to have a symmetrical operator, i.e., not depending on the scanning direction, T_2 must be equal to $1/T_1$ [28].

Ideally, the filter must be applied in all the possible directions. In practice, four direction windows are considered (see Fig. 3). The ratio is computed for each direction. The minimum ratio, corresponding to the most probable edge direction, is assigned to considered point in the ratio image.

The threshold value is obtained by making use of the model described in Section III. Such a value depends on the wind speed and on the oil film.

Use of colocated wind field is highly advisable. On this purpose, some new ideas have been proposed in literature, e.g., [40]. They are based on the physical processing of SAR images [40]. For example, some scattering approaches have been proposed. In practice, all these procedures are very much affected by SAR data calibration, uncertainties of the physical modeling and external data [41]. On the applicative viewpoint, it is also important to note that these procedures get an estimate at a scale comparable to the ones used by scatterometers. This is actually not surprising even on a physical viewpoint. In conclusion, wind field estimation from SAR image is, at the present state of the art, questionable [43].

In this paper, wind fields obtained by scatterometer data inversion are used, since they ensure high quality [27], [44]. In fact, the scatterometer is a satellite-borne active microwave remote sensor appropriately tailored to determine local wind field. As witnessed, for instance, in [45], this is not always the fact that governs SAR image formation.

On the practical viewpoint, it must be noted, however, that actual scatterometer coverage calls for interpolation procedures, and this obviously affects final quality of the wind fields. On a general perspective, one may think to refine the input parameters to the oil spill processing by means of fine physical/environmental models. Although this sounds attractive on the speculative side, it is of limited interest toward an operational use of the approach proposed in this paper. Therefore, use of mean input data and a simple filter is considered.

After edge filtering, a postprocessing can be exploited in order to make edge reconstruction [46].

V. RESULTS

In this section, we present and discuss some experiments based on SAR images acquired by Telaer consortium during the Galicia mission conducted after the Prestige sinking, off the Galicia coasts, Spain [3]. During such a mission, more than 40 SAR image acquisitions were made. The airborne SAR is an X -band system mounted onboard Learjet 35A (see Fig. 4). The most important SAR parameters are summarized in Table I. Note that full-resolution SAR images are characterized by submeter linear resolutions.

The procedure described in Section III has been tested over 40 SAR images acquired from January to February 2003. Three meaningful cases are thereafter detailed.

The first case is relevant to the sinking area characterized by large oil spills and light breeze [47]. The corresponding SAR image was acquired on 25 January 2003 at 1255 UTC to monitor

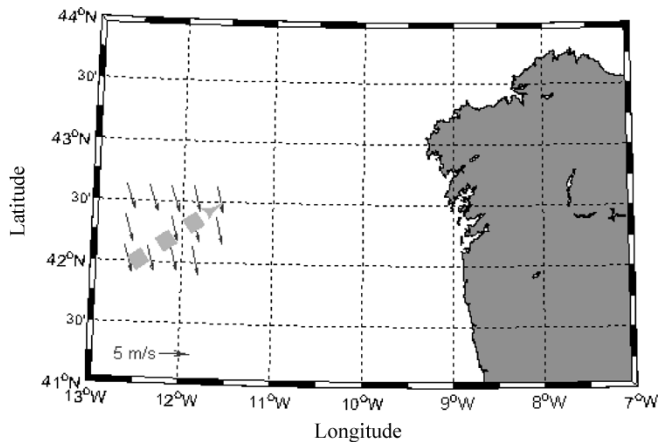


Fig. 6. Wind field obtained by inverting SeaWinds scatterometer measurements. Data are acquired on 25 January 2003 at 0541 UTC. The airplane subtrack is displayed by the hatched gray arrow.

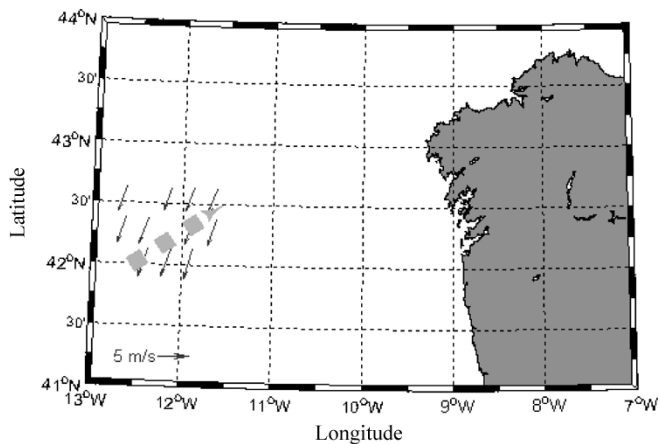


Fig. 7. Wind field obtained by inverting SeaWinds scatterometer measurements. Data are acquired on 25 January 2003 at 1935 UTC. The airplane subtrack is displayed by the hatched gray arrow.

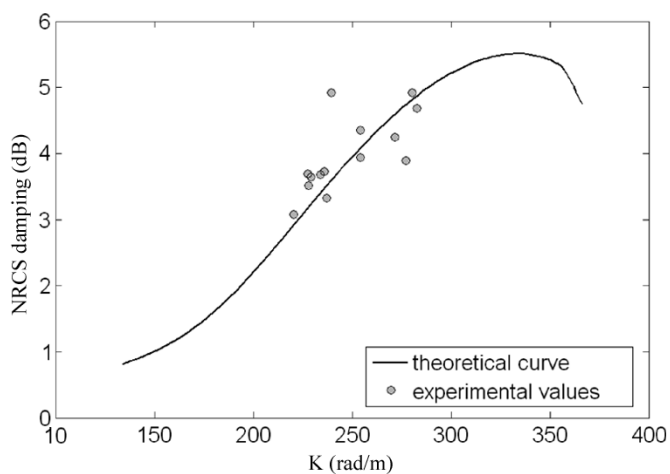


Fig. 8. Plots of the theoretical damping curve and experimental values as a function K . Wind speed of 7 m/s is considered.

the spilling out of the wreck and, therefore, to plan the counter-measure to limit further pollution. The oil spill is located around the coordinates $42^{\circ}11' \text{ N} - 12^{\circ}5' \text{ W}$ [47].

The second case is still relevant to the sinking area, and it is characterized by some oil spills of different sizes, a look-alike,

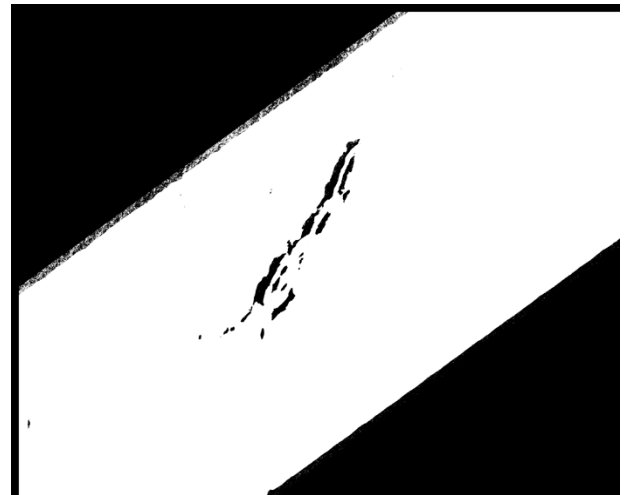


Fig. 9. Processed image relevant to the single-look SAR image corresponding to Fig. 5.



Fig. 10. Postprocessed image relevant to Fig. 9.

and light air, rough sea state. The corresponding SAR image was acquired on 16 January 2003 at 1739 UTC also to check the presence of an oil slick off the coast of Vigo (Spain) [47]. The main oil spills are located around the following coordinates: $42^{\circ}13' \text{ N} - 9^{\circ}53' \text{ W}$, $42^{\circ}13' \text{ N} - 9^{\circ}57' \text{ W}$ [47].

The third case is relevant to a large oil spill and some isolated oil spills close to some ships. These latter oil spills are most likely due to illicit oil discharge. The case is characterized by light breeze and little moved sea state [47]. The corresponding SAR image was acquired on 1 February 2003 at 1425 UTC. The main oil spill is located around the following coordinates: $42^{\circ}11' \text{ N} - 12^{\circ}1' \text{ W}$ [47].

In order to apply the oil spill processing, some input data must be provided. To make a test feasible to operational use, mean input data are considered. Wind field can be obtained by non-linear inversion of scatterometer data [27]. In this study, SeaWinds Ku -band pencil-beam scatterometer data are considered [27], [44]. In particular, wind fields corresponding to NASA SeaWinds level 3 data are exploited [27]. The level 3 data set consists of gridded values of scalar wind speeds, meridional and zonal components of wind velocity, wind speed squared, and

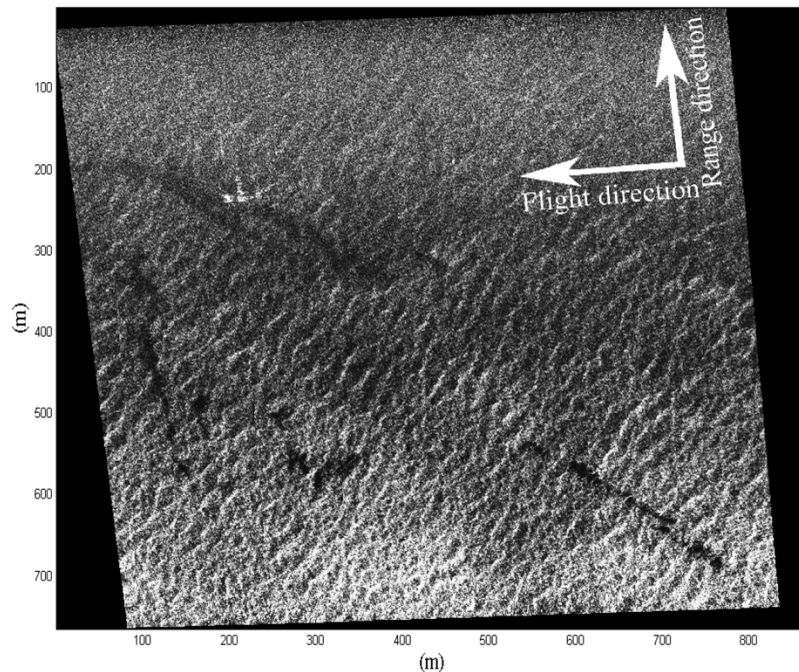


Fig. 11. SAR image acquired at X-band on 16 January 2003 at 1739 UTC, flight altitude 28 000 ft, and ground speed 150 m/s (courtesy of Telaer consortium).

time given in fraction of day. Level 3 data are provided on an approximately $0.25^\circ \times 0.25^\circ$ global grid. Separate maps are provided for both the ascending pass (6 AM LST equator crossing) and descending pass (6 PM LST equator crossing). Rain probability is also included as an indicator of wind fields reconstruction accuracy due to the presence of rain [27]. This information can also be exploited to remove from oil spill/look-alikes ambiguity due to rain cells. It must be noted, however, that our SAR measurements are not temporally coincident with scatterometer ones. Therefore, this feature is not presently included into the oil spill processing since it calls for a meteorological model.

Use of such scatterometer wind fields requires temporal interpolation, which has been performed in accordance to what was described in [48].

With respect to oil characterization, it is important to say that the oil transported by the Prestige was a heavy fuel, mainly used in industrial combustion and in slow diesel ship engines. Heavy fuel is obtained at the end of the distilling crude oil chain. In accordance to the Russian classification, this heavy fuel, with a sulphur content of 2.58%, is known as “M100,” while its English classification is “fuel oil no. 6”. It is a very viscous product at ambient temperature, considered as insoluble and characterized by a typical oil smell. More details on this oil are available in [49]. In Table II, the key mean parameters used in this study are summarized.

Let us now show the SAR images and the oil spill processing relevant to the above-mentioned three cases.

Note that for representation purposes, the SAR images are shown at quality level suitable for printing, while the SAR data used in the processing are single look, i.e., at full spatial resolution.

In Fig. 5, the SAR image corresponding to the first case is shown. Typical bright stripe due to the geometrical distortion caused by the airborne acquisition geometry can be recognized

[7]. This makes oil spill detection over airborne SAR images more challenging with respect to satellite ones. In Fig. 5, two bright spots corresponding to ships can be seen. In conjunction with this SAR image, two wind fields are taken into account (see Figs. 6 and 7). After interpolation, the estimated mean wind speed is 7 m/s [48].

Before moving to oil spill processing, it is useful to illustrate some key aspects of the physical approach. In (24), φ is set to 0° [50]. In (18), n_1 , n_2 , and d , after model calibration, are set equal to 0.01, 3.4, and 1.3, respectively. Calibration is accomplished by means of the best-fit procedure [33]. These parameters are kept constant in all subsequent experiments. Consequently, the theoretical damping curve can be plotted (see solid line in Fig. 8). The observable NRCS damping is measured over the single-look SAR image (see dots in Fig. 8). Qualitative analysis clearly shows that, once the two extreme outliers are discarded, experimental results are in excellent agreement with theoretical ones. This is confirmed by the quantitative analysis: Normalized correlation index is equal to 0.92.

Quantitative analysis also shows that the decrease of the friction velocity due to the oil spill is 3–5%.

The result of the SAR image processing (Section IV), applied over the single-look SAR image corresponding to Fig. 5, is shown in Fig. 9. Note that SAR image processing is capable to detect oil spill neglecting brightness band due to airborne acquisition geometry and ships. Processing results may appear unsatisfactory because of the edge smearing due to the ROA window size. However, this is untrue, because no postprocessing technique for edge reconstruction has been applied [46]. Postprocessing generates the image shown in Fig. 10. Features extraction can be applied over Fig. 10 to select key geometrical parameters [5]–[21].

In Fig. 11, the SAR image corresponding to the second case is shown. It is a very complex SAR image in which we have

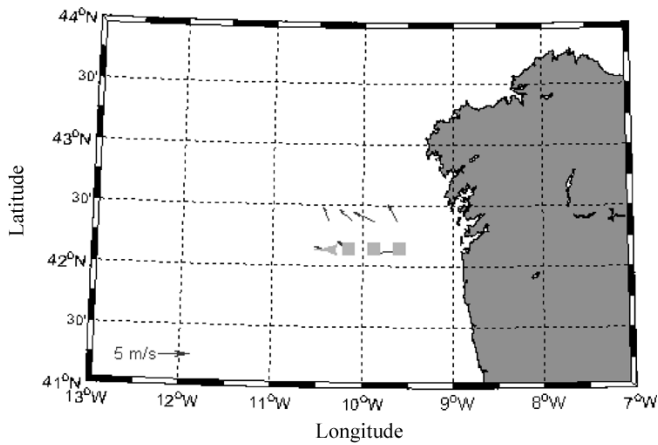


Fig. 12. Wind field obtained by inverting SeaWinds scatterometer measurements. Data are acquired on 16 January 2003 at 0613 UTC. The airplane subtrack is displayed by the hatched gray arrow.

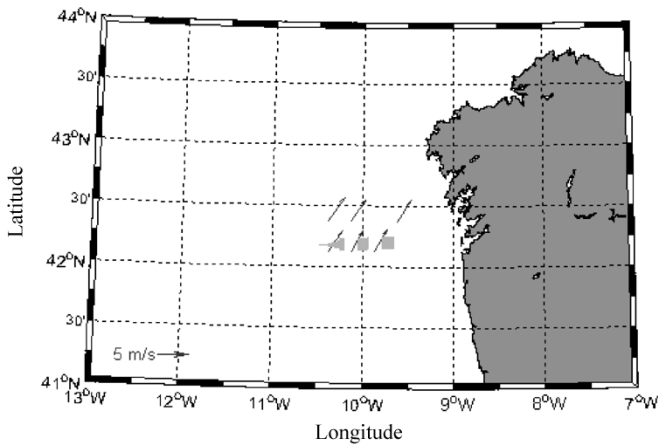


Fig. 13. Wind field obtained by inverting SeaWinds scatterometer measurements. Data are acquired on 16 January 2003 at 1827 UTC. The airplane subtrack is displayed by the hatched gray arrow.

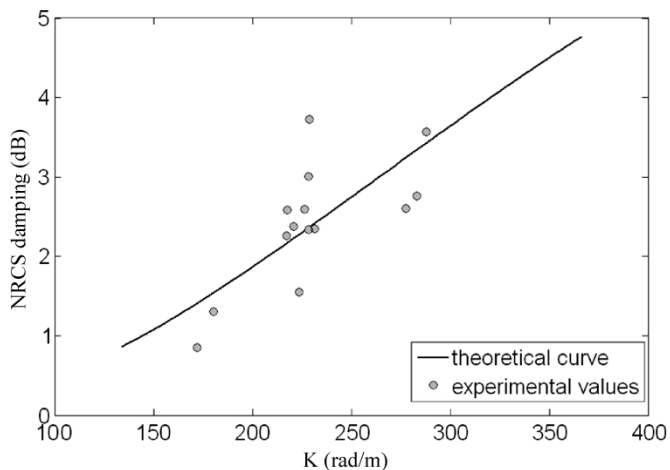


Fig. 14. Plots of the theoretical damping curve and experimental values as a function of K for the oil spills shown in Fig. 11. Wind speed of 4 m/s is considered.

multiple oil spills and a look-alike [47] in the upper left part of the image (image vertical coordinates 200–350 m and image horizontal coordinates 0–350 m).



Fig. 15. Processed image relevant to the single-look SAR image corresponding to Fig. 11.



Fig. 16. Postprocessed image relevant to Fig. 15.

A bright spot corresponding to ship can be seen. The scatterometer wind fields shown in Figs. 12 and 13 are now considered. After interpolation, the mean wind speed is 4 m/s [48].

In Fig. 14, the corresponding theoretical damping curve (solid line) and the measured observable NRCS damping (dots) are plotted. Qualitative analysis clearly shows that, once the extreme outliers are discarded, experimental results are in remarkable agreement with theoretical ones. This is confirmed by the quantitative analysis: Normalized correlation index is equal to 0.84.

The result of the SAR image processing (Section IV), applied over the single-look SAR image corresponding to Fig. 11, is shown in Fig. 15. In addition, in this case, the processing is not hampered by the brightness band due to airborne acquisition geometry. Further, ship is discarded as well as look-alike. This latter fact is of particular relevance and is due to the physically based

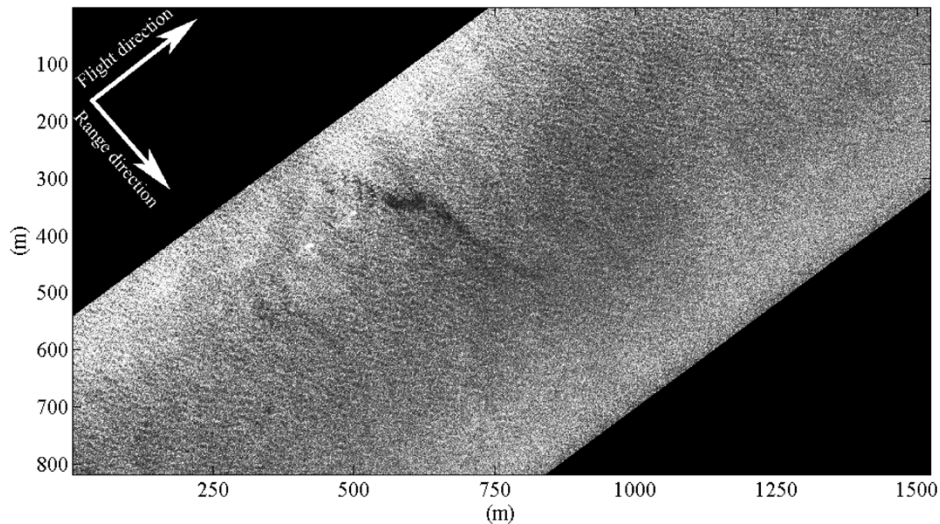


Fig. 17. SAR image acquired at X-band on 1 February 2003 at 1425 UTC, flight altitude 28 000 ft, and ground speed 150 m/s (courtesy of Telaer consortium).

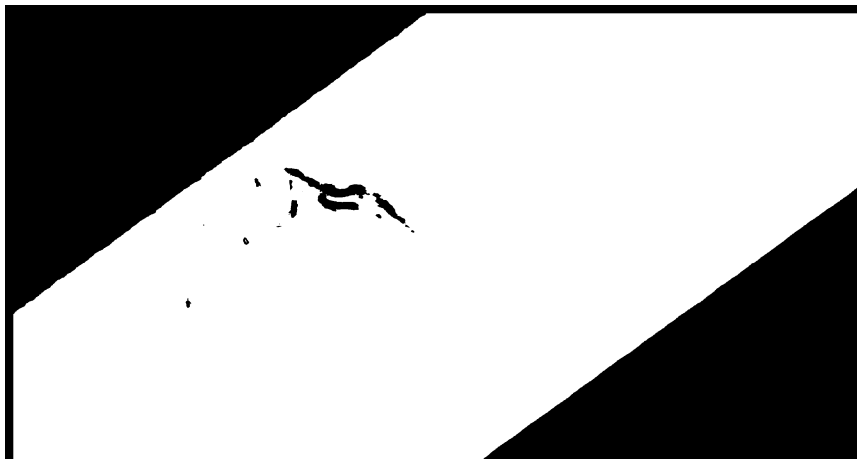


Fig. 18. Processed image relevant to single-look SAR image corresponding to Fig. 17.

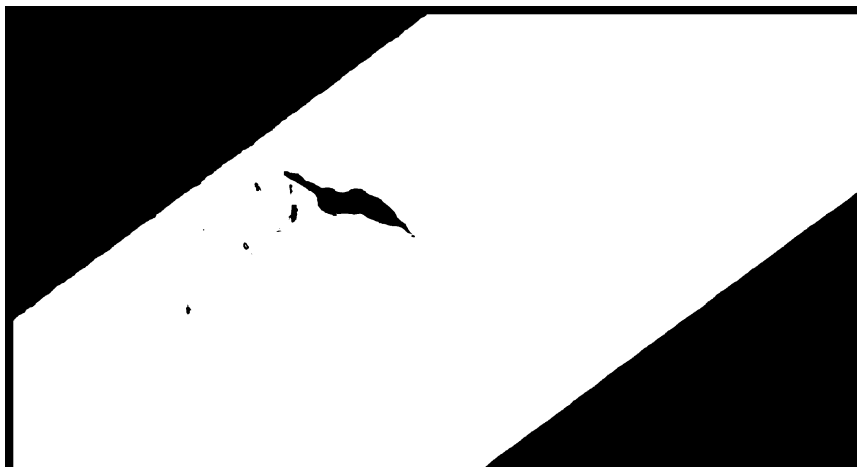


Fig. 19. Postprocessed image relevant to Fig. 18.

processing and, therefore, on the corresponding very different physical parameters. Postprocessing image is shown in Fig. 16.

In Fig. 17, the SAR image corresponding to the third case is shown. Some bright spots corresponding to ships can be seen. A large oil spill and some tankers next to the spill can be seen. Processing and postprocessing results are shown in Figs. 18 and

19, respectively. The additional information learned in this experiment is related to the capability of the oil spill processing to deal with single-look SAR images. In fact, some small-size oil spills next to the tankers are detected. They are most likely due to illegal actions and have been confirmed by other independent studies [51].

VI. CONCLUSION

Oil spill marine pollution is a matter of great concern as witnessed by the international convention for the prevention of pollution from ships, also known as MARPOL. In order to assist oil spill observation, microwave remote sensing is a valid aid since it allows actual (not nominal) continuous monitoring.

The key microwave sensor is the synthetic aperture radar (SAR). Oil spills can be detected over SAR images since they appear as dark patches. Therefore, proper processing can be applied to detect oil spills. Unfortunately, dark patches can be due to other phenomena and SAR images are affected by speckle noise.

In this paper, a new approach to oil spill processing has been presented. It is a physically based processing that incorporates available, i.e., mean, input data to a simple constant false alarm rate (CFAR) filter applicable to single-look SAR images.

The rationale of the implementation is based on a physically based approach amenable to operational use.

Numerical experiments have been accomplished over airborne X-band SAR images, which are more challenging than satellite ones.

Experimental results show that the new procedure is able to effectively process single-look SAR images. Due to the physical modeling, which takes into account the oil characteristics and the wind speed, the processing is able to discard look-alikes. In general, it can be stated that discrimination is possible when the phenomena generating a look-alike are due to physical phenomena incorporated into the observable damping model. The automatic oil spill processing is able to detect small-size oil spills.

Finally, it is noted that the oil spill processing is applicable to forthcoming remote sensing scenarios. In fact, the theory and experiments are in accordance to the planned scenario that foresees the launch of the Italian Space Agency (ASI) COSMO-SKYMED constellation, i.e., a set of X-band SARs, and the ESA Metop constellation, i.e., a set of scatterometers.

ACKNOWLEDGMENT

The authors acknowledge the Telaer consortium and Telespazio S.p.A. for providing the airborne SAR data used in this study. The Galicia mission personnel is also acknowledged for fruitful discussions. The authors also thank the reviewers for their useful suggestions.

REFERENCES

- [1] D. H. A. Al-Khudairy, "Marine Oil Pollution: Technologies and Methodologies for Detection and Early Warning," European Commission JRC, Ispra, Italy, EUR 20231 EN, 2002.
- [2] A. K. Fukuyama, G. Shigenaka, and G. R. VanBlaricom, "Oil Spill Impacts and the Biological Basis for Response Guidance: An Applied Synthesis of Research on Three Subarctic Intertidal Communities," National Oceanic and Atmospheric Administration, Seattle, WA, NOAA Tech. Memorandum NOS ORCA 125, Mar. 1998.
- [3] M. J. Caballero, "The Prestige Disaster. One Year on," Oceans Campaign, Madrid, Spain, Nov. 2003.
- [4] L. Jingxuan, H. Lim, S. Chin Liew, M. Bao, and L. K. Kwok, "Oil pollution statistics in Southeast Asian waters compiled from ERS SAR imagery," *ESA Earth Obs. Q.*, no. 61, pp. 13–17, Feb. 1999.
- [5] C. Brekke and A. H. S. Solberg, "Oil spill detection by satellite remote sensing," *Remote Sens. Environ.*, vol. 95, no. 1, pp. 1–13, Mar. 2005.
- [6] M. Migliaccio and M. Tranfaglia, "Oil spill observation by SAR: A review," in *Proc. USA-Baltic Int. Symp. "Advances in Marine Environment Res. Monitoring & Technologies"*, Klaipeda, Lithuania, Jun. 15–17, 2004.
- [7] G. Franceschetti and R. Lanari, *Synthetic Aperture Radar Processing*. Boca Raton, FL: CRC Press, 1999.
- [8] F. Li, C. Croft, and D. N. Held, "Comparison of several techniques to obtain multiple-look SAR image," *IEEE Trans. Geosci. Remote Sens.*, vol. GE-21, no. 3, pp. 370–375, Jul. 1983.
- [9] D. N. Arduin, G. Mercier, and R. Garello, "Oil slick detection by SAR imagery: Potential and limitation," in *Proc. OCEAN*, San Diego, CA, Sep. 2003, pp. 164–169.
- [10] A. Ivanov, H. E. Ming-Xia, and F. Ming-Qiang, "Oil spill detection with the RADARSAT SAR in the waters of Yellow and East China Sea: A case study," in *Proc. Asian Conf. Remote Sensing (ACRS) GIS Development*, Kathmandu, Nepal, Nov. 2002, pp. 25–29.
- [11] R. Samad and S. Mansor, "Detection of oil spill pollution using RADARSAT SAR imagery," in *Proc. Asian Conf. Remote Sensing (ACRS) GIS Development*, Kathmandu, Nepal, Nov. 2002, pp. 25–29.
- [12] M. Marghany, "RADARSAT automatic algorithms for detecting oil spill pollution," *Int. J. Appl. Earth Observ. Geoinf.*, vol. 3, no. 2, pp. 191–196, 2001.
- [13] M. Gade and W. Alpers, "Using ERS-2 SAR images for routine observation of marine pollution in European coastal water," *Sci. Total Environ.*, vol. 237–238, pp. 441–448, Sep. 1999.
- [14] A. H. S. Solberg, G. Storvik, R. Solberg, and E. Volden, "Automatic detection of oil spills in ERS SAR images," *IEEE Trans. Geosci. Remote Sens.*, vol. 37, no. 4, pp. 1916–1924, Jul. 1999.
- [15] F. Del Frate, A. Petrocchi, J. Lichtenegger, and G. Calabresi, "Neural networks for oil spill detection using ERS-SAR data," *IEEE Trans. Geosci. Remote Sens.*, vol. 38, no. 5, pp. 2282–2287, Sep. 2000.
- [16] B. Fiscella, A. Giancaspro, F. Nirchio, P. Pavese, and P. Trivero, "Oil spill detection using marine SAR images," *Int. J. Remote Sens.*, vol. 21, no. 18, pp. 3561–3566, Dec. 2000.
- [17] J. Lira and L. Frulla, "An automated region growing algorithm for segmentation of texture regions in SAR images," *Int. J. Remote Sens.*, vol. 19, no. 18, pp. 3595–3606, Dec. 1998.
- [18] A. Yessy, M. Oshima, A. Kristijono, and I. Gunawan, "Autosegmentation of oil slick in RADARSAT SAR image data around Rupert Island, Malacca Strait," in *Proc. 22nd Asian Conf. Remote Sensing*, Singapore, Nov. 5–9, 2001, pp. 1032–1036.
- [19] K. Topouzelis, V. Karathanassai, P. Pavlakis, and D. Rokos, "Oil spill detection: SAR multi-scale segmentation and object features evaluation," in *Proc. Remote Sensing Ocean and Sea Ice*, Crete, Greece, Sep. 23–27, 2002, pp. 77–87.
- [20] H. A. Espedal and T. Wahl, "Satellite SAR oil spill detection using wind history information," *Int. J. Remote Sens.*, vol. 20, no. 1, pp. 49–65, Jan. 1999.
- [21] B. Jones and E. G. Mitchelson-Jacob, "On the interpretation of SAR imagery from Sea Empress oil spill," *Int. J. Remote Sens.*, vol. 19, no. 4, pp. 789–795, Mar. 1998.
- [22] M. Gade, W. Alpers, H. Huhnerfuss, V. R. Wismann, and P. A. Lange, "On the reduction of the radar backscatter by oceanic surface films: Scatterometer measurements and their theoretical interpretation," *Remote Sens. Environ.*, vol. 66, no. 1, pp. 52–70, Oct. 1998.
- [23] M. Gade, W. Alpers, H. Huhnerfuss, H. Masuko, and T. Kobayashi, "Imaging of biogenic and anthropogenic ocean surface films by the multifrequency/multipolarization SIR-C/X-SAR," *J. Geophys. Res.*, vol. 103, no. C9, pp. 18851–18866, Aug. 1998.
- [24] S. A. Ermakov, M. Migliaccio, and M. Tranfaglia, "Oil spill observation: A physical approach," in *Proc. USA-Baltic Int. Symp. Advances Marine Environmental Research Monitoring & Technologies*, Klaipeda, Lithuania, Jun. 15–17, 2004.
- [25] S. A. Ermakov, A. M. Zujkova, A. R. Panchenko, S. G. Salashin, T. G. Talipova, and V. I. Titov, "Surface film effect on short wind waves," *Dyn. Atmos. Ocean.*, vol. 10, no. 1, pp. 31–50, Feb. 1986.
- [26] S. A. Ermakov, "Resonance damping of gravity-capillary waves on the water surface covered with a surface-active film," *Izv. Atmos. Ocean. Phys.*, vol. 39, no. 5, pp. 624–628, 2003.
- [27] SeaWinds on QuikSCAT level 3 daily, gridded ocean wind vectors, in *Physical Oceanography DAAC*, 1st ed., JPL, pp. 1–39, 2001.
- [28] R. Touzi, A. Lopes, and P. Bousquet, "A statistical and geometrical edge detector for SAR imagery," *IEEE Trans. Geosci. Remote Sens.*, vol. 26, no. 6, pp. 764–773, Nov. 1988.
- [29] R. Fjortoft, A. Lopes, P. Marthon, and E. Cubero-Castan, "An optimal multiedge detector for SAR image segmentation," *IEEE Trans. Geosci. Remote Sens.*, vol. 36, no. 3, pp. 793–802, May 1998.

- [30] O. M. Phillips, *The Dynamics of the Upper Ocean*. Cambridge, U.K.: Cambridge Univ. Press, 1966.
- [31] W. J. Plant, "A relationship between wind stress and wave slope," *J. Geophys. Res.*, vol. 87, no. C3, pp. 1961–1967, Mar. 1982.
- [32] D. Myrhaug and O. H. Slaattelid, "Effects of sea roughness and atmospheric stability on wind wave growth," *Ocean Eng.*, vol. 29, no. 9, pp. 1133–1143, Aug. 2002.
- [33] M. A. Donelan and W. J. P. Pierson, "Radar scattering and equilibrium ranges in wind-generated waves with application to scatterometry," *J. Geophys. Res.*, vol. 92, no. C5, pp. 4971–5029, May 1987.
- [34] F. T. Ulaby, R. K. Moore, and A. K. Fung, *Microwave Remote Sensing: Active and Passive*. Norwood, MA: Artech House, 1986.
- [35] A. K. Fung, *Microwave Scattering and Emission Models and Their Applications*. Norwood, MA: Artech House, 1994.
- [36] V. Hesany, R. K. Moore, S. P. Gogineni, and J. C. Holtzman, "Slope-induced nonlinearities on imaging of ocean waves," *IEEE J. Ocean Eng.*, vol. 16, no. 3, pp. 279–284, Jul. 1991.
- [37] G. Franceschetti, A. Iodice, D. Riccio, G. Ruello, and R. Siviero, "SAR raw signal simulation of oil slicks in ocean environments," *IEEE Trans. Geosci. Remote Sens.*, vol. 40, no. 9, pp. 1935–1949, Sep. 2002.
- [38] W. K. Pratt, *Digital Image Processing*. New York: Wiley, 1991.
- [39] M. Abramowitz and I. Stegun, *Handbook of Mathematical Functions*. New York: Dover, 1972.
- [40] F. Monaldo and V. Kerbaol, "The SAR measurements of ocean surface winds: An overview," in *Proc. 2nd Workshop Coastal and Marine Applications*, Swalbard, Norway, Jun. 2004, pp. 15–32.
- [41] P. W. Vachon and F. W. Dobson, "Validation of wind vector retrieval from ERS-1 SAR images over the ocean," *Global Atmos. Ocean Syst.*, vol. 5, pp. 177–187, 1996.
- [42] —, "Wind retrieval from RADARSAT SAR images: Selection of a suitable C-band HH-polarization wind retrieval model," *Can. J. Remote Sens.*, vol. 26, no. 4, pp. 306–313, Aug. 2000.
- [43] M. Migliaccio and A. Reppucci, "Una discussione sulla determinazione del campo di vento sulla superficie del mare mediante scatterometro e SAR," *Atti della Fondazione Giorgio Ronchi*.
- [44] A. Reppucci and M. Migliaccio, "SeaWinds data inversion," *Atti della Fondazione Giorgio Ronchi*, no. 4, 2005.
- [45] R. H. Stewart, *Methods of Satellite Oceanography*. Berkeley, CA: Univ. of California Press, 1985.
- [46] J. R. Parker, *Algorithms for Image Processing and Computer Vision*. New York: Wiley, 1997.
- [47] Telaer Data Analysis Report, Feb. 2003.
- [48] *Off-Line Wind Scatterometer ERS Products—User Manual (V2.1)*, CERSAT-IFREMER, Plouzane, France, Jan. 1999.
- [49] <http://www.etcentre.org> [Online]
- [50] J. R. Apel, *Principles of Ocean Physics*. New York: Academic, 1990.
- [51] R. Garelo, private communication, Jun. 2004.



Maurizio Migliaccio (M'91–SM'00) was born and educated in Italy.

He is a Full Professor of electromagnetics at Università degli Studi di Napoli "Parthenope," Napoli, Italy, where he teaches microwave remote sensing. He participated in the international NASA-ASI-DARA project on synthetic aperture radar (SAR) interferometry. He was a Visiting Scientist at DLR, Weßling, Germany. He was UE Secretary of the COST 243 action. His current remote sensing research activities deal with electromagnetic modeling, oil spills SAR monitoring, wind scatterometer data inversion, and spatial resolution enhancement of radiometric data.

Prof. Migliaccio was a member of the Università degli Studi di Napoli Parthenope Ad Com. He is a member of the AGU and the Italian remote sensing association (AIT). He is Chairman of the IEEE GRS South Italy Chapter.



Massimo Tranfaglia (S'03) was born in Avellino, Italy, on April 8, 1978. He received the M.S. degree (5-year legal course of study) in nautical science (summa cum laude) from the Università degli Studi di Napoli "Parthenope," Napoli, Italy, in 2003. He is working toward the Ph.D. degree in information engineering at the Università degli Studi del Sannio, Benevento, Italy.

His main research interest are in the field of synthetic aperture radar (SAR) polarimetry, radio detection and ranging (RADAR) signal processing, mathematical and physical modeling of microwave scattering, and oil spill monitoring by means of SAR.



Stanislav A. Ermakov was born in Gorky, now Nizhny Novgorod, Russia. He received the Honoured Diploma in radiophysics from Gorky University, Nizhny Novgorod, Russia, in 1973, and the Ph.D. degree in geophysics from the Marine Hydrophysical Institute, Sevastopol, Ukraine, in 1981.

He first worked at the Radiophysical Research Institute, and since 1978, he has been with the Institute of Applied Physics (IAP), Russian Academy of Sciences, Nizhny Novgorod, Russia. He is currently Head of Laboratory of radar probing of the sea surface.

His main research interests are in the fields of hydrodynamics of surface and internal waves in the ocean, marine slicks, and ocean remote sensing. He has been studying the problems in theory and in field and wave tank experiments.